J. Fluid Mech. (2020), *vol.* 891, R5, doi:10.1017/jfm.2020.202

JFM RAPIDS
journals.cambridge.org/rapids

Reduced flow reversals in turbulent convection in the absence of corner vortices

Xin Chen[1], **Dong-Pu Wang**[1] **and Heng-Dong Xi**[1,†]

[1]School of Aeronautics, Northwestern Polytechnical University, Xi'an, 710072, PR China

(Received 23 December 2019; revised 24 February 2020; accepted 10 March 2020)

We report a comparative experimental study of the reversal of the large-scale circulation in turbulent Rayleigh–Bénard convection in a quasi-two-dimensional corner-less cell where the corner vortices are absent and in a quasi-two-dimensional normal cell where the corner vortices are present. It is found that in the corner-less cell the reversal frequency exhibits a slow decrease followed by a fast decrease with increasing Rayleigh number Ra, separated by a transitional Ra ($Ra_{t,r}$). The transition is similar to that in the normal cell, and $Ra_{t,r}$ is almost the same for both cells. Despite the similarities, the reversal frequency is greatly reduced in the corner-less cell. The reduction of the reversal frequency is more significant, in terms of both the amplitude and the scaling exponent, in the high-Ra regime. In addition, we classified the reversals into main-vortex-led and corner-vortex-led, and found that both types exist in the normal cell while only the former exists in the corner-less cell. The frequency of main-vortex-led reversal in the normal cell is found to be in excellent agreement with the frequency of reversals in the corner-less cell. Our results reveal for the first time the quantitative role of the corner vortices in the occurrence of the reversals of the large-scale circulation.

Key words: Bénard convection, turbulent convection, vortex interactions

1. Introduction

Rayleigh–Bénard (RB) convection, a fluid layer heated from below and cooled from above (see Ahlers, Grossmann & Lohse 2009; Lohse & Xia 2010; Chilla & Schumacher 2012; Xia 2013), continues to attract great attention not only for its relevance to widely occurring convection phenomena in nature, such as the motion of the Earth's mantle and outer core, the winds in the atmosphere and the currents in the oceans, but also because it is a paradigm for the study of buoyancy-driven turbulence. RB convection is characterized by the Rayleigh number $Ra = \alpha g \Delta T H^3/(\nu\kappa)$, and the Prandtl number $Pr = \nu/\kappa$, where H is the height of the convection cell, ΔT

† Email address for correspondence: hengdongxi@nwpu.edu.cn

is the temperature difference between the bottom and top plates of the convection cell, g is the gravitational acceleration, and α, ν and κ are, respectively, the volume expansion coefficient, kinematic viscosity and thermal diffusivity of the fluid. When Ra exceeds a critical value, the hot and cold plumes erupted from the bottom and top plates interact with each other and evolve into a large-scale circulation (LSC), which takes the form of a single roll (Krishnamurti & Howard 1981; Cioni, Ciliberto & Sommeria 1997; Xi, Lam & Xia 2004). A fascinating feature of the LSC is the spontaneous and random reversal of its flow direction. The reversal of the LSC is of general interest for its putative connection (Sreenivasan, Bershadskii & Niemela 2002; Araujo, Grossmann & Lohse 2005; Benzi 2005; Brown, Nikolaenko & Ahlers 2005; Xi & Xia 2007, 2008; Sugiyama *et al.* 2010) to similar reversals in the atmosphere (van Doorn *et al.* 2000), or in the outer core of the Earth (Glatzmaier *et al.* 1999). Despite the extensive studies in the last two decades (Sreenivasan *et al.* 2002; Araujo *et al.* 2005; Benzi 2005; Brown *et al.* 2005; Sugiyama *et al.* 2010; Chandra & Verma 2013; Ni, Huang & Xia 2015; Podvin & Sergent 2015; Castillo-Castellanos, Sergent & Rossi 2016; Huang & Xia 2016; Horstmann, Schiepel & Wagner 2018; Wang *et al.* 2018*a*,*b*; Castillo-Castellanos *et al.* 2019; Chen *et al.* 2019), a general understanding of the mechanism of the reversal of the LSC remains elusive.

In studies of the reversal of the LSC, very often (quasi-) two-dimensional (2-D) rectangular convection cells are used (Liu & Zhang 2008; Sugiyama *et al.* 2010; Huang *et al.* 2015; Ni *et al.* 2015; Wang *et al.* 2018*a*), because in the (quasi-) 2-D cell the influence of the three-dimensional dynamic features of the LSC, such as the torsional and sloshing motions that are typically found in a cylindrical geometry (Funfschilling & Ahlers 2004; Brown *et al.* 2005; Xi *et al.* 2009, 2016), are eliminated. In the (quasi-) 2-D geometry, the LSC consists of a big main vortex of a tilted ellipse shape and two small corner vortices diagonally opposite to each other. It was found that the reversal of the LSC is accomplished as follows: the corner vortices grow in both size and amplitude, squeeze and eventually break up the main vortex, then connect to each other to form a new big single-roll vortex again, but with a reversed circulating direction (Sugiyama *et al.* 2010; Chandra & Verma 2013). In this picture the corner vortices play a crucial role in the reversal process. However, it was recently found in a vertical thin circular cell, where the corner vortices are absent, that the reversal of the LSC could still occur (Wang *et al.* 2018*b*). It was also found that the scaling of the reversal frequency versus Ra is controlled by the stability of the main vortex (Chen *et al.* 2019). To unlock the intricate dynamics behind these seemingly contradictory results, a comparative study of the reversals in cells with and without corner vortices becomes essential.

In this paper, we report a comparative experimental study of the reversals of the LSC in a corner-less and a normal convection cell. It is found that in the corner-less cell the reversal of LSC still happens, and the reversal frequency decreases with Ra, and is divided into slow and fast decrease regimes. The transition of the reversal frequency in this corner-less cell is very similar to that in the normal cell, while the reversal frequency in the corner-less cell is greatly reduced. The reduction of the reversal frequency is more significant, in terms of both the amplitude and the scaling exponent, in the high-Ra regime. It is found that the reversals can be classified into main-vortex-led (MVL) and corner-vortex-led (CVL), and both types exist in the normal cell while only the former exists in the corner-less cell. The frequency of MVL reversal in the normal cell is found to be in excellent agreement with the frequency of reversals in the corner-less cell. Our results reveal, for the first time, the quantitative role of the corner vortices in the occurrence of the reversals of the LSC.

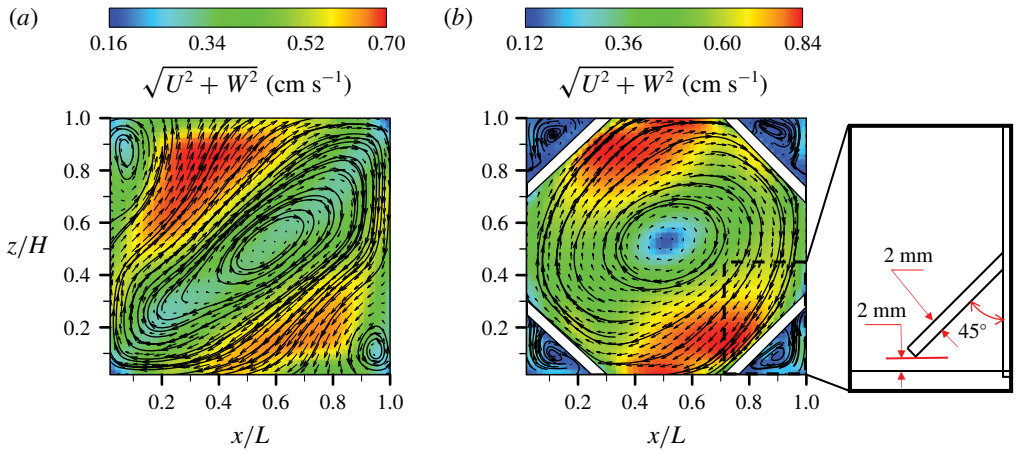

FIGURE 1. Long-time-averaged particle image velocimetry velocity map with streamlines measured from (*a*) the normal cell at $Ra = 7.94 \times 10^8$ and (*b*) the corner-less cell at $Ra = 7.56 \times 10^8$, both at $Pr = 7.0$. The velocity is coded with both colour and vector length in units of cm s^{-1}. Also shown is a sketch of one corner of the corner-less cell.

2. Experimental set-up and methods

Two types of convection cells, i.e. the normal cell and the corner-less cell, were used in our experiments. The two types of cells differ only in that there are four additional Plexiglas plates at the four corners in the corner-less cell but were otherwise identical. The height (H), length (L) and width (W) of the cells are 12.6 cm, 12.6 cm and 3.8 cm, respectively; thus the aspect ratios are $L/H = 1$ and $W/L = W/H \simeq 0.3$. The normal cell has been described elsewhere (Chen *et al.* 2019). Here, we only mention some essential features. The convection cell consists of copper top and bottom plates and the Plexiglas sidewall. The temperature of the top plate was controlled by a refrigerated circulator (Polyscience) and the bottom plate is heated by two resistive film heaters with constant power input. In each plate, there are six thermistors of 2.5 mm diameter embedded to measure the temperature. The three pairs of thermistors are equally spaced along the L direction at $L/4$, $L/2$ and $3L/4$, and we refer them as left, middle and right. To separate the main vortex and the corner vortex, at each of the four corners we glue a 2 mm thick Plexiglas plate, as shown in figure 1(*b*) where the side view of one corner is sketched. The plate is 3.8 cm in width and 4.5 cm long. The angles between the Plexiglas plate and the bottom (top) plate and the vertical sidewall are both 45°; thus the projections of the plate on both the bottom (top) plate and vertical sidewall are roughly $H/4$. Three of the four edges of each of the plates are in close contact (glued) with the three inner faces of the Plexiglas sidewalls; only the bottom (top) edge is 2 mm away from the bottom (top) fluid–plate interface. With the Plexiglas plates at the four corners, the bulk flow largely feels no corners, while the 2 mm gap allows exchange of heat and mass between the fluid flow inside the corner and bulk fluid flow. The gap height is comparable to the thickness of the thermal boundary layer in our experiments. To test whether the shape of the plates affects the results, we have also performed experiments with four concavely curved plates with the same projections on the plates and the sidewalls. Although the curved plates give a slightly more circular interior of the cell, we found the results are very similar to those obtained by the flat plates.

Deionized water was used as the working fluid and the experiments in the corner-less cell were conducted in the Ra range of 9.58×10^7 to 3.71×10^8 for $Pr = 5.7$ and 1.03×10^8 to 5.59×10^8 for $Pr = 7.0$. Owing to the small lateral aspect ratio $W/H \simeq 0.3$, the LSC is confined in the vertical L–H plane; the cell is thus considered quasi-2-D (Xia, Sun & Zhou 2003). To detect the reversal of LSC, we use the temperature contrast method (Sugiyama *et al.* 2010; Ni *et al.* 2015; Huang & Xia 2016; Chen *et al.* 2019), i.e. identify the reversal event through the temperature contrast δ between the thermistors embedded on the left and right sides of the plates, $\delta = T_{left} - T_{right}$. To have enough statistics, each measurement lasts for 1–2 days; the longest measurement lasted continuously for 15 days. The criteria used to identify the reversal event can be found in Huang & Xia (2016) and Chen *et al.* (2019). They are based on the amplitude and duration time of δ. The first criterion is that the two circulation states of the LSC (clockwise direction and anticlockwise direction) should be clearly distinguished from each other. This implies that the probability density function (p.d.f.) of δ (see figure 2*d* of Huang & Xia (2016)) should have two peaks (two most probable values) with each peak corresponding to one circulation state, and the distance d between the two peaks in the p.d.f. should be larger than the root mean squared (r.m.s.) value of δ, so that the two peaks can be clearly distinguished (note that here the peak value corresponds to the threshold in Castillo-Castellanos *et al.* (2019)). The second criterion is that when the flow changes from one state to the other, δ should first cross over the peak corresponding to the current state, then cross over the peak corresponding to the other state, i.e. the value of δ should be larger (smaller) than the higher (lower) peak value of δ in the p.d.f. The third criterion is that the flow should stay at the new state for more than one turnover time of the LSC. The second criterion has guaranteed that the reversal is not the cessation observed in the simulation of 2-D RB convection by Castillo-Castellanos *et al.* (2019).

3. Results and discussion

3.1. *Flow topology and scaling of the global quantities*

We first compare the flow topology in the normal and the corner-less cells. Figure 1(*a*,*b*) shows the time-averaged velocity field captured in the normal and the corner-less cells at similar Ra (7.94×10^8 and 7.56×10^8, respectively) for $Pr = 7.0$; and during the 2 hours average time, no reversal occurs. From figure 1(*a*), one can see that the typical flow pattern in the normal cell consists of a main vortex in the shape of a tilted ellipse and two small corner vortices sitting at the top-left and bottom-right corners, which is consistent with previous studies (Xia *et al.* 2003; Sugiyama *et al.* 2010). In the corner-less cell, the flow pattern is totally different, due to the existence of the Plexiglas plates. The main vortex feels no corners, thus it is in a circular shape. The fluid trapped in the corners is heated up (cooled down) by the bottom (top) plate, goes up (down) due to the buoyancy force, and is then deflected and comes down (goes up) due to the existence of the Plexiglas plates and the sidewall. After that it is heated up (cooled down) and goes up (comes down) again, thus forming fixed-size small vortices, which are isolated from the bulk fluid. There is almost no mass or momentum transfer between these isolated corner vortices and the main vortex except for the greatly reduced heat, mass and momentum transfer through the 2 mm thick gap. Although the Plexiglas plate is a poor thermal conductor (with thermal conductivity of 0.19 W m^{-1} K^{-1}), as it is very thin (2 mm), presumably there is still strong heat transfer between the fluid trapped

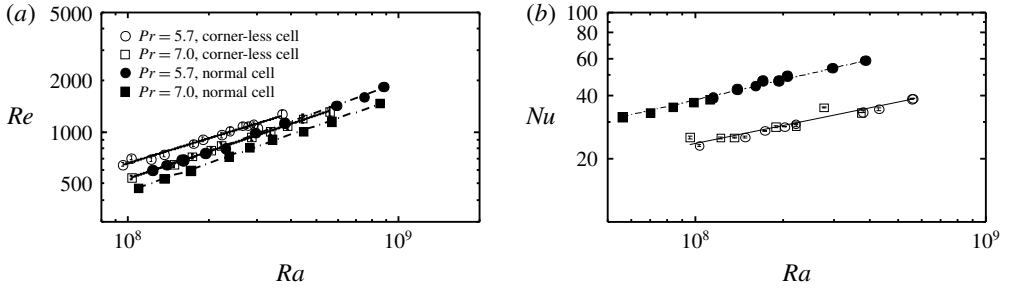

FIGURE 2. Plots of (*a*) *Re* and (*b*) *Nu* as functions of *Ra* for $Pr = 5.7$ and 7.0 from the normal and the corner-less cells. The solid and dashed lines are power-law fits to the corresponding data.

in the corner and the bulk fluid through the Plexiglas plate. The size of these corner rolls behind the Plexiglas plates is fixed, determined by the size of the Plexiglas plates. Nevertheless, with the addition of the four Plexiglas plates, an LSC without (the effects of) the corner vortices is indeed achieved. It should be emphasized that the fixed-size 'corner vortices' in the corner-less cell are totally different from the corner vortices in the normal cell. In the normal cell the corner vortices can directly interact with the main vortex: they can grow and squeeze the main roll and connect with each other to form a new main vortex.

We then characterize the corner-less convection system by studying the scaling properties of the global quantities such as Reynolds number *Re* and Nusselt number *Nu*, which quantifies the heat transfer efficiency and is defined as the ratio between the total heat flux across the system and the heat flux by pure conduction in the fluid. Figure 2(*a*) shows the measured *Re* as a function of *Ra* for $Pr = 5.7$ and 7.0 in the normal and the corner-less cells. Here, $Re = 4H^2/(\nu t_E)$, where t_E is the turnover time of the LSC; t_E is obtained by the cross-correlation of temperature signals inside the top and the bottom plates. It is well known that the LSC is an organized motion of thermal plumes. When the LSC sweeps on the conducting plates, it will lead to a local temperature fluctuation and pass its signature to the boundaries. Such a signature can be detected not only in the sidewall but also in the top and bottom plates (Cioni *et al.* 1997; Brown, Funfschilling & Ahlers 2007; Xi *et al.* 2009; Wei *et al.* 2014). It can be seen from figure 2(*a*) that *Re* measured in the corner-less cell is approximately 20 % higher than that in the normal cell for both $Pr = 5.7$ and 7.0. This increased *Re* implies a stronger LSC in the corner-less cell, as now there are no corner vortices to drain energy from the main vortex. In spite of the higher amplitude of *Re* in the corner-less cell, the scalings of *Re* versus *Ra* for both cells are almost the same, as shown by the solid and dashed lines in figure 2(*a*); they exhibit almost the same scalings, $Re \sim Ra^{0.55}$. And the scaling exponent obtained here are consistent with previous results in similar normal cells (Xia *et al.* 2003; Zhou, Sun & Xia 2007; Zhang, Zhou & Sun 2017).

Figure 2(*b*) shows the measured $Nu = J/(\chi \Delta T/H)$ as a function of *Ra* in both normal and corner-less cells, where *J* and χ are the total heat flux entering the convection cell and the thermal conductivity of water. The relation can be described by $Nu \sim Ra^{0.30}$ for the normal cell and by $Nu \sim Ra^{0.28}$ for the corner-less cell. The scaling exponents are consistent with previous results in similar normal cells (Ciliberto, Cioni & Laroche 1996; Huang & Xia 2016; Jiang *et al.* 2018). Although

the scaling exponents are very close to each other for both cells, the amplitude of Nu is much smaller in the corner-less cell; it is only approximately 60 % of the value in the normal cell. The reduction of Nu should be due to the fact that some of the heat supplied in the corner region is trapped by the Plexiglas plates, and thus cannot be transported to the main flow. Moreover, it also implies that the corner vortices play an important role in terms of heat transfer in the normal cell (Huang & Zhou 2013).

Note that, in the corner-less cell, part of the heating and cooling surfaces are not accessible to the bulk fluid due to the existence of the Plexiglas plate; thus the effective heating area is reduced compared to the normal cell case. Therefore, the effective Nu based on this reduced heating area will be much larger. The total heat flux is $J = (U^2/R)/A$, where U is the voltage applied on the heater in the bottom plate, R is the resistance of the heater embedded in the bottom plate and A is the surface area of the bottom plate. For the sake of clarity, we define Nu measured in the normal cell as Nu_n and that measured in the corner-less cell as Nu_{cl}. If we take the area that is not covered by the Plexiglas plate as the effective heating area, which is roughly $0.5A$, the effective Nu_{eff} will be $Nu_{cl}/0.5 = 2Nu_{cl}$. As we already knew that $Nu_{cl} = 0.6Nu_n$, thus $Nu_{eff} = 1.2Nu_n$. That is, compared to the Nu measured in the normal cell, the effective Nu measured in the corner-less cell is increased by 20 %. This seems consistent with the 20 % increase of Re.

3.2. *The reversal frequency*

Previously, in the normal cell, we (Chen *et al.* 2019) have found that there is a transition in the Ra dependence of the reversal frequency f with two distinct scalings: for Ra less than a transitional Ra, the non-dimensionalized reversal rate $ft_E \sim Ra^{-1.09}$; for higher Ra, however, the scaling changes to $ft_E \sim Ra^{-3.06}$. Flow visualization shows that this regime transition originates from a transition in flow topology from the normal single-roll state (SRS) to the abnormal single-roll state (ASRS) with substructures inside the single roll. The emergence of the substructures inside the LSC lowers the energy barrier for the flow reversals to occur and leads to a slower decay of f with Ra. Detailed analysis reveals that, although it is the corner vortices that trigger the reversal event, the probability for the occurrence of reversals mainly depends on the stability of the LSC (Chen *et al.* 2019).

We now examine the reversal frequency f in the corner-less cell, where f is defined as the averaged number of reversal events per second. Figure 3(*a*,*b*) shows the normalized f as a function of Ra in the corner-less cell for $Pr = 5.7$ and 7.0, respectively. For comparison, f measured in the normal cell (Chen *et al.* 2019) and in a vertical circular thin disk (Wang *et al.* 2018*b*) are also plotted. To compare f in the different systems, we non-dimensionalize it by $1/t_E$. From figure 3(*a*,*b*), one can see that f in the corner-less cell decreases with Ra, i.e. it is harder and harder for reversal to occur with increasing Ra, which is consistent with that in the normal cell (Chen *et al.* 2019) and in the circular thin disk (Wang *et al.* 2018*b*). Moreover, f measured in the corner-less cell also exhibits a transition with two distinct regimes separated by a transitional Ra ($Ra_{t,r}$): a slow decay regime and a fast decay regime, which is also consistent with that in the normal cell (Chen *et al.* 2019). It is seen from figure 3(*a*,*b*) that $Ra_{t,r}$ measured in the corner-less cell is almost the same as that in the normal cell (for the same Pr). We note that f measured in the thin circular disk also scales with Ra, and the scaling exponent is very close to that of the normal/corner-less cell in the $Ra < Ra_{t,r}$ (or ASRS) regime. This implies that in the Ra range of the vertical thin circular disk experiment (Wang *et al.* 2018*b*), the large-scale flow should be in

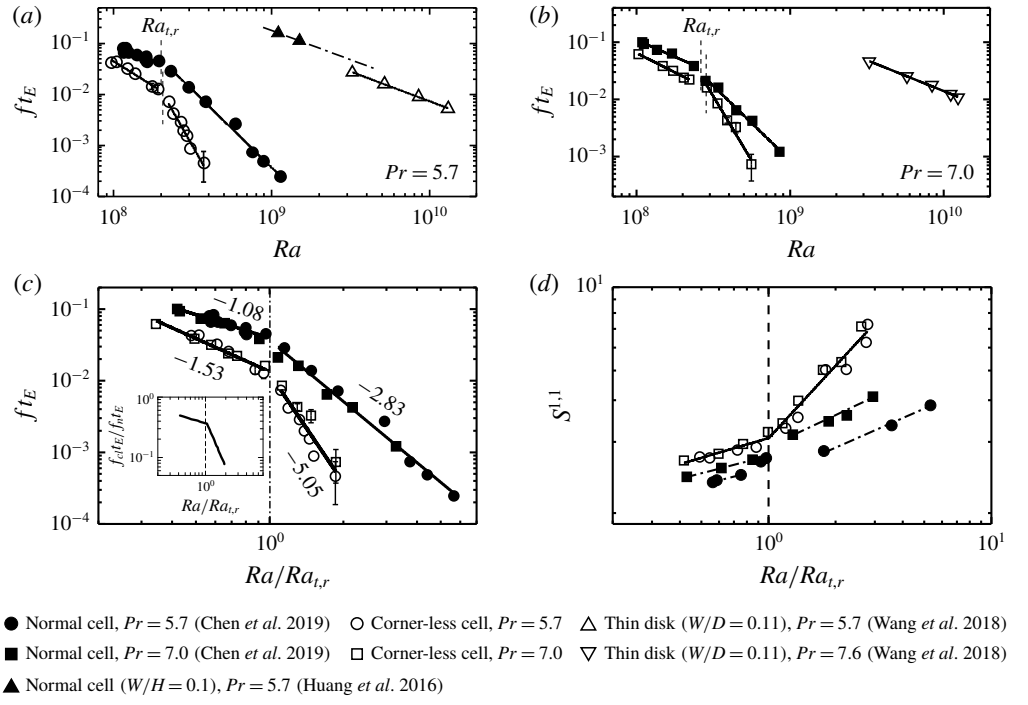

FIGURE 3. Flow reversal frequency f (normalized by $1/t_E$) as a function of Ra for $Pr = 5.7$ (a) and $Pr = 7.0$ (b). Reversal frequency measured in a vertical thin circular disk ($W/D = 0.11$) at $Pr = 5.7$ and 7.6 by Wang *et al.* (2018*b*), and in the normal cell ($W/H = 0.1$) at $Pr = 5.7$ by Huang & Xia (2016) are also plotted for comparison. (c) The same data as in (a) and (b), but Ra is normalized by $Ra_{t,r}$, with $Ra_{t,r} = 2.0 \times 10^8$ for $Pr = 5.7$ and 3.0×10^8 for $Pr = 7.0$. Inset: the ratio of the reversal frequency in the corner-less cell $f_{cl}t_E$ to that in the normal cell f_nt_E. (d) The stability of the (1, 1) mode $S^{1,1} = \langle A^{1,1} \rangle / \sigma_{A^{1,1}}$ as a function of normalized Ra. In (a–d), the solid lines are the power-law fits to the data and the vertical dashed lines indicate the transitional Rayleigh number $Ra_{t,r}$.

the ASRS regime, i.e. the interior of the LSC is already broken into two smaller vortices. And $Ra_{t,r}$ for the thin circular disk should be very high, which is reasonable, as in this thin circular disk the aspect ratio Γ = thickness/diameter is very small ($\Gamma = 0.11$) compared to $\Gamma = W/H \simeq 0.3$ in our cell. Thus the viscous damping due to the sidewalls is much stronger; as a result, the transitional Ra is much larger (Chen *et al.* 2019). We expect that if we normalize Ra for the thin circular disk data by its own $Ra_{t,r}$, the data would collapse with the data from the corner-less cell in the $Ra < Ra_{t,r}$ regime; unfortunately the $Ra_{t,r}$ for this geometry is not known to us.

Also plotted in figure 3(a) is f measured in a $W/H = 0.1$ (almost the same aspect ratio as in Wang *et al.* (2018*b*)) normal cell by Huang & Xia (2016). Although we have only two data points and the Ra range does not overlap with that of Wang *et al.* (2018*b*), if we fit the two data points with a straight line then extend to the Ra range of Wang *et al.* (2018*b*), it is found that the reversal frequency in the normal cell is higher than that in the circular disk. This is consistent with our results that (for the same aspect ratio) the reversal frequency is higher in cells with corner vortices. In figure 3(c) we plot f as a function of Ra for the two different Pr together, where Ra is normalized by $Ra_{t,r}$. For comparison, the data from the normal cell (Chen *et al.*

2019) are also plotted. As shown in figure 3(*c*), similar to the normal cell case, the data from the corner-less cell fall on top of each other with two distinct scaling regimes being $ft_E \sim Ra^{-1.53\pm0.12}$ and $ft_E \sim Ra^{-5.05\pm0.18}$. The existence of the transition for both cases, with and without the corner vortices, confirms that the transition originates from the stability of the main vortex (Chen *et al.* 2019).

Compared to that in the normal cell, f in the corner-less cell is greatly reduced, as shown by the ratio of normalized reversal frequency $(f_{cl}t_E)/(f_nt_E)$ in the inset of figure 3(*c*); here f_{cl} and f_n are the reversal frequencies from the corner-less and the normal cells, respectively, and the values of $f_{cl}t_E$ and f_nt_E are from the power-law fitting in figure 3(*c*). On average the reversal frequency is reduced by approximately 50 % when $Ra < Ra_{t,r}$, and by approximately 90 % when $Ra > Ra_{t,r}$. On the other hand, the decay rate of f with Ra is also changed: in the $Ra < Ra_{t,r}$ regime, the scaling exponent is changed from -1.08 to -1.53; while in the $Ra > Ra_{t,r}$ regime, it is changed from -2.83 to -5.05. One can see that the scaling exponent in the $Ra < Ra_{t,r}$ regime does not change as much as that in the $Ra > Ra_{t,r}$ regime. The reason is understandable: when $Ra < Ra_{t,r}$, the LSC is in the ASRS, where the interior of the main vortex is already broken into two small vortices (Chen *et al.* 2019); thus it is very unstable. In this regime, the reversal is mainly induced by the instability of the main vortex, and the corner vortex does not play a significant role. Thus when the corner vortices are eliminated, the decay rate of the reversal frequency does not change much. This regime is referred to as the MVL reversal dominant regime. When $Ra > Ra_{t,r}$, the flow is in the SRS, the main vortex is very stable and it is very hard for the reversal to occur if there are no corner vortices to drain energy from, and weaken and break the main vortex. In this regime the corner vortices are significant to the occurrence of the reversal. Thus, once the corner vortices are eliminated, the reversal frequency is greatly reduced. This regime is referred to as the CVL reversal dominant regime.

3.3. *The transition of the flow topology and the stability of the LSC*

Previously, in the normal cell, it has been shown that the transition in the reversal frequency originates from the flow topology transition from the ASRS to the SRS (Chen *et al.* 2019). To examine whether the reversal frequency transition in the corner-less cell is from the same origin, we study the flow topology evolution with Ra in the corner-less cell. The particle image velocimetry (PIV) technique is used to measure the flow field of the vertical mid-plane in the corner-less cell. For each Ra, the PIV measurements last for at least 2 hours and at least 7200 snapshots were acquired at 1 Hz sampling rate. Figure 4 shows the evolution of the short-time-averaged flow field with Ra for $Pr = 7.0$. It is very similar to the case in the normal cell (Chen *et al.* 2019): when $Ra \leqslant 3.0 \times 10^8$ (figure 4*a–c*), the flow is in the ASRS, i.e. a single roll with substructure in it; when $Ra > 3.0 \times 10^8$ (figure 4*d–f*), the flow is in the SRS, i.e. a single roll without any substructures in it. The transitional Ra for the flow topology is almost the same as $Ra_{t,r}$ determined from the reversal frequency. It is also found that a similar flow topology transition happens in the $Pr = 5.7$ case as well. Thus we come to the conclusion that the transition of the reversal frequency ft_E in the corner-less cell also originates from the transition of flow topology. In a previous study, we have proposed a model to predict the critical condition for the interior of the LSC to break, based on the balance between advection and viscous dissipation of thermal plumes (Chen *et al.* 2019). As the model does not depend on the geometry of the cell, it also applies to the corner-less cell.

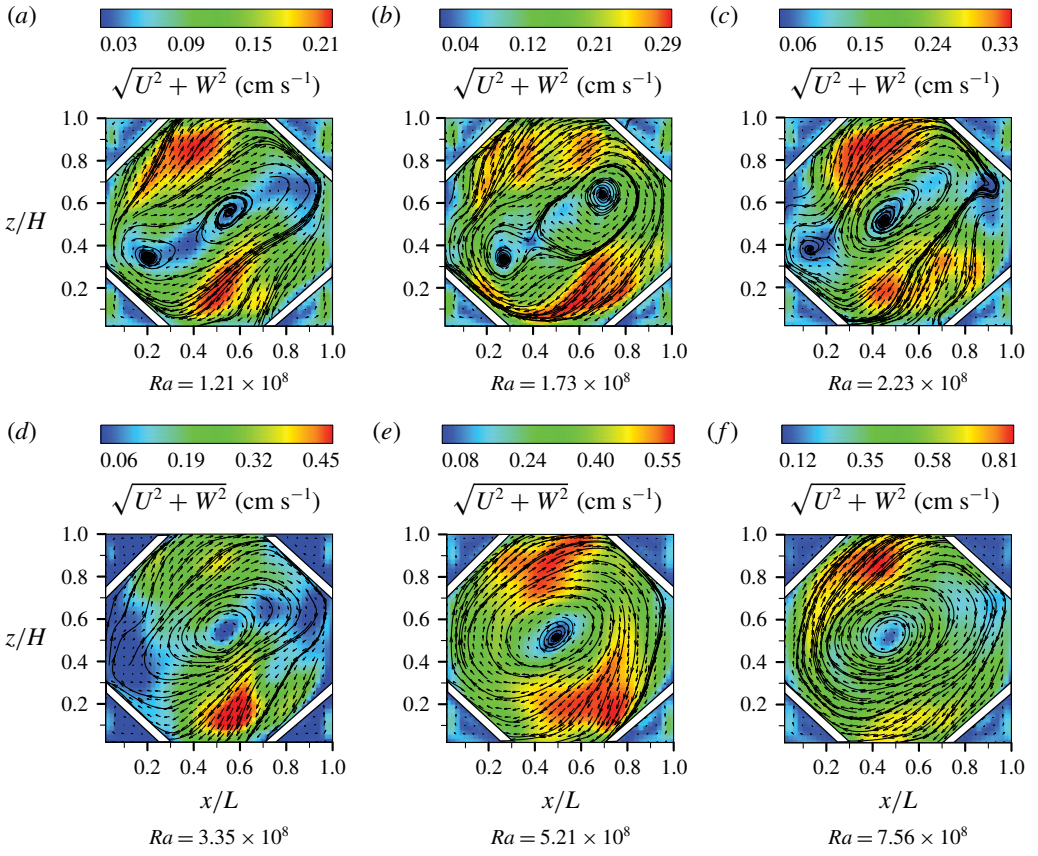

FIGURE 4. Flow topology evolution with increasing Ra in the corner-less cell. Short-time-averaged (within one LSC turnover time t_E) PIV velocity maps with streamlines at different Ra (as indicated) for $Pr = 7.0$. The velocity is coded with both colour and vector length in units of cm s^{-1}. Here the streamlines inside each corner are not shown.

To gain a quantitative understanding of the flow evolution with Ra in the corner-less cell, we decompose the instantaneous PIV velocity map into Fourier modes (Chandra & Verma 2013; Wagner & Shishkina 2013; Wang *et al.* 2018*a*). The Fourier mode decomposition has been introduced in detail in Chen *et al.* (2019). Briefly, we project the velocity map (u_x, u_z) onto the following Fourier basis: $u_x^{m,n} = 2\sin(m\pi x)\cos(n\pi z)$, $u_z^{m,n} = -2\cos(m\pi x)\sin(n\pi z)$. The values $m, n = 1, 2, 3$ are considered. The so-obtained mode (m, n) corresponds to a flow field with m rolls in the x direction and n rolls in the z direction. For example, the (1, 1) mode is the single-roll mode. The amplitude of the Fourier mode $A^{m,n}$ is obtained by the component-wise projection of each velocity map on the Fourier basis. To apply the Fourier mode decomposition in the corner-less cell, we set the velocity vectors inside the corners to be zero. It was previously shown that, in the normal cell, the slow (fast) decay of the reversal frequency in the $Ra < Ra_{t,r}$ ($Ra > Ra_{t,r}$) regime is due to the slow (fast) increase of the stability of the (1, 1) mode of the flow, where the stability of the (1, 1) mode is defined as its mean amplitude divided by its r.m.s. value $S^{1,1} = \langle A^{1,1}\rangle/\sigma_{A^{1,1}}$ (Chen *et al.* 2019). As can be seen from figure 3(*d*), similar to the case in the normal cell, $S^{1,1}$ first experiences a slow increase, followed by a fast increase. And the transitional Ra for $S^{1,1}$ is almost

identical to that for reversal frequency. It should be noted that, in the $Ra < Ra_{t,r}$ regime, the increasing rates of $S^{1,1}$ from the normal cell and from the corner-less cell are very close to each other. Since the stability of the (1, 1) mode controls the decay rate of the reversal frequency, the decay rates of the reversal frequency in the normal cell and the corner-less cell are very close to each other as well, as shown in figure 3(*c*). While in the $Ra > Ra_{t,r}$ regime, $S^{1,1}$ increases much faster in the corner-less cell, which explains why the reversal frequency decays much faster than that in the normal cell. The one-to-one correspondence between the increasing rate of $S^{1,1}$ and the decay rate of reversal frequency in both the corner-less cell and the normal cell reveals that the decay rate is indeed controlled by the stability of the (1, 1) mode (the main vortex).

3.4. *The main-vortex-led and the corner-vortex-led reversals*

As we mentioned before, in the normal cell, when $Ra < Ra_{t,r}$ the reversals are MVL dominant, and when $Ra > Ra_{t,r}$ the reversals are CVL dominant. It is natural to ask whether it is possible to distinguish the MVL reversals from the CVL reversals in the normal cell. In addition, as in the corner-less cell the corner vortices are eliminated, the reversals in this geometry should be all MVL. One would expect that the reversal frequency in the corner-less cell should behave similarly as the MVL reversals in the normal cell. To answer these questions, we examine the duration time t_d of the reversals, i.e. the time it takes for the flow to switch from one direction to the other direction. In the normal cell, when $Ra < Ra_{t,r}$, as the interior of the main vortex is already broken, the breakdown time of the main vortex and the reversal process should not take long; when $Ra > Ra_{t,r}$, the main vortex is very stable, it takes some time for the corner vortices to drain energy from the main vortex, then grow, and weaken then break the main vortex – thus it will take a longer time for the reversal to be accomplished. We found that it is indeed the case that the averaged duration time t_d/t_E increases with Ra, and $t_d/t_E < 1$ when $Ra < Ra_{t,r}$ (MVL reversal dominant) and $t_d/t_E > 1$ when $Ra > Ra_{t,r}$ (CVL reversal dominant). Another more direct way to examine the average behaviour of t_d is to show the ensemble-averaged time traces of δ during the reversals (see Xi *et al.* (2016) for details on the calculation of the ensemble average). In figure 5(*a*,*b*) we show the ensemble-averaged temperature difference $\widetilde{\delta}(t)$ for the MVL reversal dominant regime ($Ra = 1.15 \times 10^8 < Ra_{t,r}$) and the CVL reversal dominant regime ($Ra = 2.96 \times 10^8 > Ra_{t,r}$), respectively. The ensemble average was performed for the 1405 reversal events identified for $Ra = 1.15 \times 10^8$ and for the 217 reversal events identified for $Ra = 2.96 \times 10^8$. It is found that indeed in the MVL reversal dominant regime it takes a much shorter time ($\sim 0.4t_E$) for the reversal to be accomplished, compared to that in the CVL dominant regime ($\sim 3t_E$).

In figure 5(*c*) we plot the p.d.f. of t_d (normalized by t_E) for two Ra ($Ra = 1.15 \times 10^8$ and 2.96×10^8, both at $Pr = 5.7$) that straddle $Ra_{t,r}$ ($= 2.0 \times 10^8$). In our experiments, these two Ra are furthest away from $Ra_{t,r}$ and at the same time have enough reversal events for statistical analysis. It is found that for $Ra\,(= 1.15 \times 10^8) < Ra_{t,r}$, where MVL dominates, the p.d.f. of t_d is peaked in the small t_d range with peak value approximately $0.15t_E$, while for $Ra\,(= 2.96 \times 10^8) > Ra_{t,r}$, where CVL dominates, the p.d.f. of t_d is peaked in the large t_d range with peak value approximately $1.45t_E$. We have checked the other Ra: they all show similar behaviour. Since the above two Ra are furthest away from each other and straddle $Ra_{t,r}$, we decided to use the median value of the two peaks as the separation t_d between the MVL and the CVL reversals, which is $0.8t_E$. By using this criterion we sort the reversal events

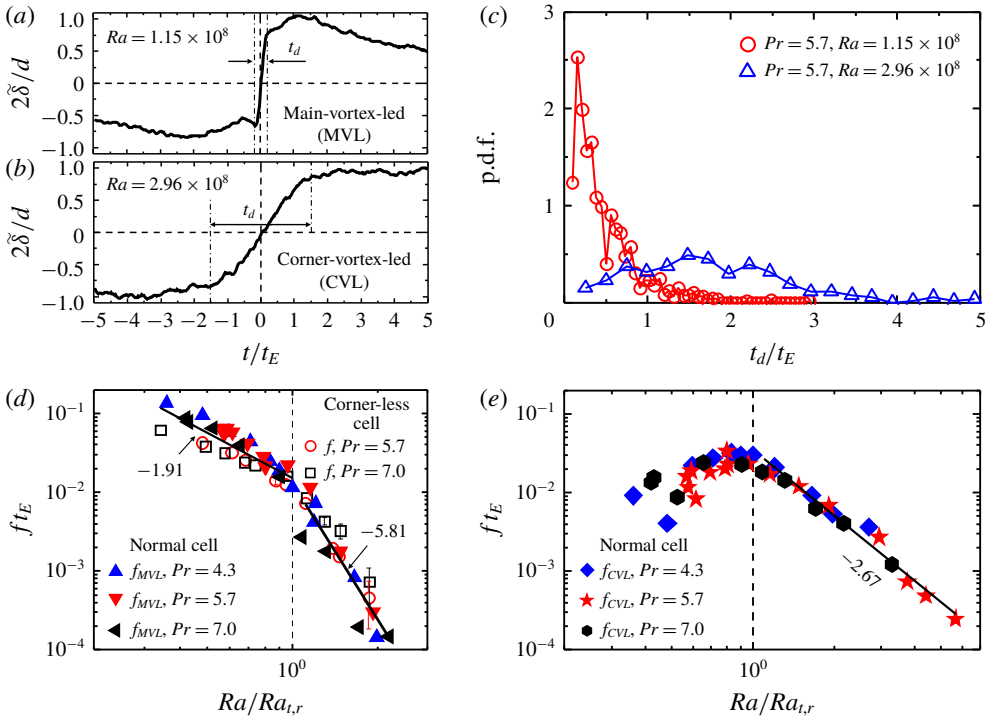

FIGURE 5. (*a*,*b*) Ensemble-averaged time traces of temperature difference $\widetilde{\delta}$ (normalized by $d/2$) during reversal for the normal cell when (*a*) $Ra = 1.15 \times 10^8 < Ra_{t,r}$ and (*b*) $Ra = 2.96 \times 10^8 > Ra_{t,r}$, respectively. Here d is the peak-to-peak separation of the p.d.f. of δ; d is 0.012 K for (*a*) and 0.015 K for (*b*), respectively. (*c*) The p.d.f. of the normalized duration time of reversal t_d/t_E for the normal cell at $Ra = 1.15 \times 10^8$, $Pr = 5.7$, where MVL reversal dominates, and at $Ra = 2.96 \times 10^8$, $Pr = 5.7$, where CVL reversal dominates. The two Ra straddle $Ra_{t,r}$ $(= 2.0 \times 10^8)$. (*d*,*e*) The frequencies of the MVL reversal f_{MVL} (*d*) and the CVL reversal f_{CVL} (*e*) as a function of Ra from the normal cell. Also plotted in (*d*) is the reversal frequency f from the corner-less cell. The solid lines are the power-law fits to the data. Note that in (*d*) the data from both the normal cell and the corner-less cell are included for the fit.

into the MVL and CVL. We then obtain the reversal frequencies f_{MVL} for MVL reversals and f_{CVL} for CVL reversals. In figure 5(*d*) we plot the Ra dependence of f_{MVL} from the normal cell; also plotted is f from the corner-less cell, where all the reversals have to be MVL. It is found that f_{MVL} and f agree not only in the trend but also in amplitude, which reveals that the reversals are indeed controlled by the stability of the main vortex (MVL) in the low-Ra regime, and by the destabilization of the corner vortices (CVL) in the high-Ra regime, and by using the corner-less cell the latter was almost eliminated. In figure 5(*e*) we plot f_{CVL} from the normal cell. It is found that the frequency of CVL reversal slowly increases when $Ra < Ra_{t,r}$, then decreases in a power-law manner with scaling exponent -2.67. As for very high Ra range ($Ra \gg Ra_{t,r}$) in the normal cell, all the reversals are CVL; thus f and f_{CVL} should be the same and it is indeed the case in terms of both the scaling exponents (-2.83 versus -2.67) and the amplitude.

4. Summary and discussion

In summary, we have designed a corner-less cell where the corner vortices are eliminated. A comparative study was performed in the corner-less cell and the normal cell. It is found that the reversal of the LSC could also happen in the absence of the corner vortices. In the corner-less cell, overall the reversal frequency decreases with *Ra*, and it shows a slow decrease followed by a fast decrease, which is consistent with the case in normal cells. Detailed flow visualization reveals that the transition of the reversal frequency in the corner-less cell also originates from the transition of the flow topology from the abnormal single-roll state to the normal single-roll state, like that in the normal cell. The reversal frequency in the corner-less cell is greatly reduced. The reduction of the reversal frequency is more significant, in terms of both the amplitude and the scaling exponent, in the high-*Ra* regime, which reveals that the corner vortices play a more important role in the high-*Ra* regime. The reason is that in the high-*Ra* regime the main vortex is very strong and stable, unless there are some external disturbances to destabilize the main vortex; otherwise it is very hard for the reversal to occur. The corner vortices actually are such external disturbances: they drain energy from the very strong main vortex, weaken and destabilize it, and promote the occurrence of reversals. While in the low-*Ra* regime, the corner vortices are not significant because the main vortex itself is unstable. The instability of the main vortex is enough to accomplish a reversal without the help of the corner vortices. Our results reveal that, although the corner vortices are not necessary for the reversal, the presence of the corner vortices greatly increases the reversal frequency through destabilizing the main vortex, especially in the high-*Ra* regime.

Acknowledgements

We thank P. Tong and Y. Wang for sharing with us the reversal frequency data in their vertical thin circular disk. We are grateful for stimulating discussions with D. Lohse, H. Hu, J. Zhang, K.-Q. Xia and S.-D. Huang, and for support by the NNSF of China (grant nos 11772259 and U1613227), the '111 Project' of China (B17037) and the Fundamental Research Funds for the Central Universities of China (no. 3102019PJ002).

Declaration of interests

The authors report no conflict of interest.

References

Ahlers, G., Grossmann, S. & Lohse, D. 2009 Heat transfer and large scale dynamics in turbulent Rayleigh–Bénard convection. *Rev. Mod. Phys.* **81** (2), 503–537.

Araujo, F. F., Grossmann, S. & Lohse, D. 2005 Wind reversals in turbulent Rayleigh–Bénard convection. *Phys. Rev. Lett.* **95** (8), 084502.

Benzi, R. 2005 Flow reversal in a simple dynamical model of turbulence. *Phys. Rev. Lett.* **95** (2), 024502.

Brown, E., Funfschilling, D. & Ahlers, G. 2007 Anomalous Reynolds-number scaling in turbulent Rayleigh–Bénard convection. *J. Stat. Mech.: Theory Exp.* **2007** (10), P10005–P10005.

Brown, E., Nikolaenko, A. & Ahlers, G. 2005 Reorientation of the large-scale circulation in turbulent Rayleigh–Bénard convection. *Phys. Rev. Lett.* **95** (8), 084503.

Castillo-Castellanos, A., Sergent, A., Podvin, B. & Rossi, M. 2019 Cessation and reversals of large-scale structures in square Rayleigh–Bénard cells. *J. Fluid Mech.* **877**, 922–954.

CASTILLO-CASTELLANOS, A., SERGENT, A. & ROSSI, M. 2016 Reversal cycle in square Rayleigh–Bénard cells in turbulent regime. *J. Fluid Mech.* **808**, 614–640.

CHANDRA, M. & VERMA, M. K. 2013 Flow reversals in turbulent convection via vortex reconnections. *Phys. Rev. Lett.* **110** (11), 114503.

CHEN, X., HUANG, S.-D., XIA, K.-Q. & XI, H.-D. 2019 Emergence of substructures inside the large-scale circulation induces transition in flow reversals in turbulent thermal convection. *J. Fluid Mech.* **877**, R1.

CHILLA, F. & SCHUMACHER, J. 2012 New perspectives in turbulent Rayleigh–Bénard convection. *Eur. Phys. J.* E **35**, 58 (2012).

CILIBERTO, S., CIONI, S. & LAROCHE, C. 1996 Large-scale flow properties of turbulent thermal convection. *Phys. Rev.* E **54** (6), R5901–R5904.

CIONI, S., CILIBERTO, S. & SOMMERIA, J. 1997 Strongly turbulent Rayleigh–Bénard convection in mercury: comparison with results at moderate Prandtl number. *J. Fluid Mech.* **335**, 111–140.

VAN DOORN, E., DHRUVA, B., SREENIVASAN, K. R. & CASSELLA, V. 2000 Statistics of wind direction and its increments. *Phys. Fluids* **12** (6), 1529–1534.

FUNFSCHILLING, D. & AHLERS, G. 2004 Plume motion and large-scale circulation in a cylindrical Rayleigh–Bénard cell. *Phys. Rev. Lett.* **92** (19), 194502.

GLATZMAIER, G. A., COE, R. S., HONGRE, L. & ROBERTS, P. H. 1999 The role of the Earth's mantle in controlling the frequency of geomagnetic reversals. *Nature* **401** (6756), 885–890.

HORSTMANN, G. M., SCHIEPEL, D. & WAGNER, C. 2018 Experimental study of the global flow-state transformation in a rectangular Rayleigh–Bénard sample. *Intl J. Heat Mass Transfer* **126**, 1333–1346.

HUANG, S.-D., WANG, F., XI, H.-D. & XIA, K.-Q. 2015 Comparative experimental study of fixed temperature and fixed heat flux boundary conditions in turbulent thermal convection. *Phys. Rev. Lett.* **115** (15), 154502.

HUANG, S.-D. & XIA, K.-Q. 2016 Effects of geometric confinement in quasi-2D turbulent Rayleigh–Bénard convection. *J. Fluid Mech.* **794**, 639–654.

HUANG, Y.-X. & ZHOU, Q. 2013 Counter-gradient heat transport in two-dimensional turbulent Rayleigh–Bénard convection. *J. Fluid Mech.* **737**, R3.

JIANG, H.-C., ZHU, X.-J., MATHAI, V., VERZICCO, R., LOHSE, D. & SUN, C. 2018 Controlling heat transport and flow structures in thermal turbulence using ratchet surfaces. *Phys. Rev. Lett.* **120** (4), 044501.

KRISHNAMURTI, R. & HOWARD, L. N. 1981 Large-scale flow generation in turbulent convection. *Proc. Natl Acad. Sci. USA* **78** (4), 1981–1985.

LIU, B. & ZHANG, J. 2008 Self-induced cyclic reorganization of free bodies through thermal convection. *Phys. Rev. Lett.* **100** (24), 244501.

LOHSE, D. & XIA, K.-Q. 2010 Small-scale properties of turbulent Rayleigh–Bénard convection. *Annu. Rev. Fluid Mech.* **42** (1), 335–364.

NI, R., HUANG, S.-D. & XIA, K.-Q. 2015 Reversals of the large-scale circulation in quasi-2D Rayleigh–Bénard convection. *J. Fluid Mech.* **778**, R5.

PODVIN, B. & SERGENT, A. 2015 A large-scale investigation of wind reversal in a square Rayleigh–Bénard cell. *J. Fluid Mech.* **766**, 172–201.

SREENIVASAN, K. R., BERSHADSKII, A. & NIEMELA, J. J. 2002 Mean wind and its reversal in thermal convection. *Phys. Rev.* E **65**, 056306.

SUGIYAMA, K., NI, R., STEVENS, R. J., CHAN, T.-S., ZHOU, S.-Q., XI, H.-D., SUN, C., GROSSMANN, S., XIA, K.-Q. & LOHSE, D. 2010 Flow reversals in thermally driven turbulence. *Phys. Rev. Lett.* **105** (3), 034503.

WAGNER, S. & SHISHKINA, O. 2013 Aspect-ratio dependency of Rayleigh–Bénard convection in box-shaped containers. *Phys. Fluids* **25** (8), 085110.

WANG, Q., XIA, S.-N., WANG, B.-F., SUN, D.-J., ZHOU, Q. & WAN, Z.-H. 2018*a* Flow reversals in two-dimensional thermal convection in tilted cells. *J. Fluid Mech.* **849**, 355–372.

WANG, Y., LAI, P.-Y., SONG, H. & TONG, P. 2018*b* Mechanism of large-scale flow reversals in turbulent thermal convection. *Sci. Adv.* **4** (11), eaat7480.

WEI, P., CHAN, T.-S., NI, R., ZHAO, X.-Z. & XIA, K.-Q. 2014 Heat transport properties of plates with smooth and rough surfaces in turbulent thermal convection. *J. Fluid Mech.* **740**, 28–46.

XI, H.-D., LAM, S. & XIA, K.-Q. 2004 From laminar plumes to organized flows: the onset of large-scale circulation in turbulent thermal convection. *J. Fluid Mech.* **503**, 47–56.

XI, H.-D. & XIA, K.-Q. 2007 Cessations and reversals of the large-scale circulation in turbulent thermal convection. *Phys. Rev.* E **75**, 066307.

XI, H.-D. & XIA, K.-Q. 2008 Azimuthal motion, reorientation, cessation, and reversal of the large-scale circulation in turbulent thermal convection: a comparative study in aspect ratio one and one-half geometries. *Phys. Rev.* E **78**, 036326.

XI, H.-D., ZHANG, Y.-B., HAO, J.-T. & XIA, K.-Q. 2016 Higher-order flow modes in turbulent Rayleigh–Bénard convection. *J. Fluid Mech.* **805**, 31–51.

XI, H.-D., ZHOU, S.-Q., ZHOU, Q., CHAN, T.-S. & XIA, K.-Q. 2009 Origin of the temperature oscillation in turbulent thermal convection. *Phys. Rev. Lett.* **102** (4), 044503.

XIA, K.-Q. 2013 Current trends and future directions in turbulent thermal convection. *Theor. Appl. Mech. Lett.* **3** (5), 052001.

XIA, K.-Q., SUN, C. & ZHOU, S.-Q. 2003 Particle image velocimetry measurement of the velocity field in turbulent thermal convection. *Phys. Rev.* E **68**, 066303.

ZHANG, Y., ZHOU, Q. & SUN, C. 2017 Statistics of kinetic and thermal energy dissipation rates in two-dimensional turbulent Rayleigh–Bénard convection. *J. Fluid Mech.* **814**, 165–184.

ZHOU, S.-Q., SUN, C. & XIA, K.-Q. 2007 Measured oscillations of the velocity and temperature fields in turbulent Rayleigh–Bénard convection in a rectangular cell. *Phys. Rev.* E **76**, 036301.